AIAA JOURNAL
Vol. 48, No. 6, June 2010

Effects of Flexible Fin on Low-Frequency Oscillation in Poststall Flows

Tianshu Liu,* J. Montefort,† W. Liou,‡ and S. Pantula§
Western Michigan University, Kalamazoo, Michigan 29008

DOI: 10.2514/1.J050205

This paper discusses the effects of a thin flexible rectangular polymer film (fin) attached to the upper surface of a NACA0012 airfoil model on the natural low-frequency oscillation in poststall flows. The flexible fin passively manipulates flow structures, which leads to suppression of the low-frequency oscillation and reduction of drag. Detailed measurements of the velocity fields and kinematics of fin deformation show the significant effects of a flexible fin on the development of the flow structures in the fully-separated-flow region. The generating and controlling mechanisms of the low-frequency oscillation are explored.

I. Introduction

FLOW separation control is of immense importance to the performance of air vehicles and other technologically important systems involving fluids. Generally, it is desired to postpone separation such that the form drag is reduced, stall is delayed, lift is enhanced, and pressure recovery is improved. Therefore, a great effort has been made over years in flow separation control (or stall control) of airfoils and wings by using various techniques [1–14]. In general, separation control has been achieved by either injecting high-momentum fluid into separated-flow regions or removing low-momentum fluid from the separated flows for angles of attack (AOA) that are smaller than or near stalled AOA. It has been demonstrated that a partially separated flow can be almost reattached by unsteady forcing, and stall is delayed. Effective control of poststall flows fully separated from the leading edge over airfoils remains challenging. Poststall flows over airfoils contain not only the vortical structures developed in the separated shear layer, but also the natural low-frequency oscillation. The low-frequency oscillation has been observed in wind-tunnel testing and for a long time mistakenly considered as a phenomenon mainly related to elastic structure. Zaman et al. [15] systematically studied the natural low-frequency oscillation of a LRN(1)-1007 airfoil and other airfoils near stall and demonstrated it as a fluid-mechanical phenomenon. They also suggested that it might be due to switching between stalled and unstalled flows. Bragg et al. [16,17] and Broeren and Bragg [18,19] conducted studies on unsteady stalling of a LRN(1)-1007 airfoil and provided experimental evidences on the combination of the thin-airfoil stall with a leading-edge separation bubble and the trailing-edge stall as a mechanism of the low-frequency oscillation. Large-eddy simulation for a LRN(1)-1007 airfoil has captured some qualitative characteristics of the low-frequency oscillation observed in experiments [20].

The possible regimes of flow patterns over thin airfoils in terms of AOA and Reynolds number are shown in Fig. 1, which is similar to that given by Wu et al. [21]. The low-frequency oscillation has been observed in the dashed-line-marked regime in Fig. 1. Data of the stall AOA in $Re_c = 3 \times 10^4$–10^7 are collected from [22,23], and those in $Re_c = 2 \times 10^3$–2×10^4 are from [24–26]. The region marked by the dashed line indicates a possible regime in which the natural low-frequency oscillation occurs. Data from the experiments of Zaman et al. [15] and Bragg et al. [16,17] and Broeren and Bragg [18,19] are marked in the diagram. The cases of the low-frequency oscillation investigated in the present work are also marked with filled circles in Fig. 1.

Zaman et al. [15,27] studied the effects of acoustic excitation on stalled flows over an airfoil, and found that acoustic excitation at high frequencies (hundreds times higher than those of the low-frequency oscillation) mysteriously precipitated the low-frequency oscillation. In contrast, screen-generated turbulence and acoustic excitation with lower frequencies only slightly augmented the low-frequency oscillation. No clear explanation on the physical mechanisms behind these findings was given. Control of stalled flows using periodic blowing and suction near the leading edge of a NACA0012 airfoil was numerically simulated by Wu et al. [21], where the excitation is typically based on the vortex-shedding mode. They found that the lift could be increased by this unsteady forcing to promote the formation of concentrated lifting vortices. The drag could be increased or reduced depending on the forcing frequency and AOA. For example, forcing at the subharmonic frequency of the vortex-shedding mode led to the largest lift increase, but the drag is also considerably increased. In contrast, the largest drag reduction was found under forcing at 4 times of the vortex-shedding frequency, but the lift enhancement is small. The effects of the forcing on the vorticity structures and interactions between the forcing and the leading-edge shear layer were studied. However, Wu et al. [21] did not particularly address control of the low-frequency oscillation. In fact, there is still a lack of a systematic investigation on control of the low-frequency oscillation at poststall AOA.

Inspired by the observation that the feathers on the upper surface of a bird's wing tend to pop up during landing or in gusty winds, Bechert et al. [28], Bramesfeld and Maughmer [29], and Meyer et al. [30] used movable semirigid flaps near the trailing edge of a wing to enhance the lift near stall. Tests in wind tunnels showed that the maximum lift coefficient could be significantly increased by deploying the flaps acting as dams blocking the reversed flow from moving further upstream for certain thick airfoils where separation starts from the trailing edge. A thin plate on a NACA0012 airfoil has been also used to delay the bursting of laminar separation bubbles [31].

In this study, a flexible rectangular polymer film attached to the upper surface of an airfoil is used, which is called fin (it could be also called flipper or flap). Although the fin is similar to the movable flaps proposed by Bechert et al. [28], our focus is on passive control of the low-frequency oscillation in poststall flows over a NACA0012 airfoil

Received 10 September 2009; revision received 20 December 2009; accepted for publication 30 January 2010.

*Professor, Department of Mechanical and Aeronautical Engineering, Room G-220, Parkview Campus; tianshu.liu@wmich.edu. Senior Member AIAA (Corresponding Author).

†Assistant Professor, Department of Mechanical and Aeronautical Engineering.

‡Professor, Department of Mechanical and Aeronautical Engineering. Associate Fellow AIAA.

§Graduate Research Assistant, Department of Mechanical and Aeronautical Engineering.

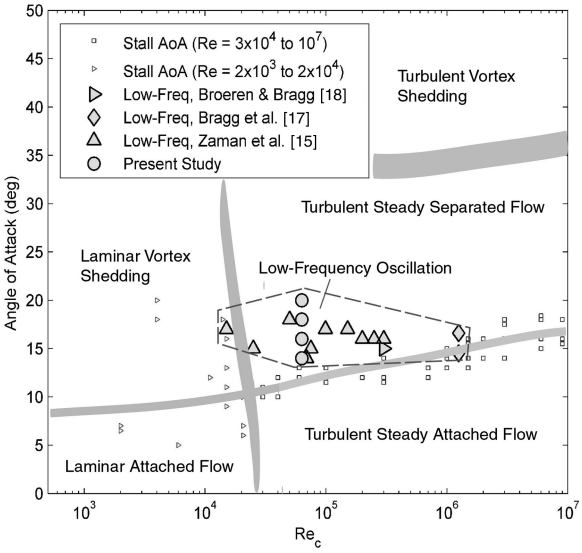

Fig. 1 Diagram of stall regimes.

model. In particular, we are interested in interactions of a flexible fin with the vortical structures in the separated shear layer and the resulting global effects on the whole fully-separated-flow region. For this purpose, unlike the movable flaps installed near the trailing edge, a thin flexible fin is typically attached to the upper surface near the leading edge of an airfoil. Figure 2a illustrates a thin flexible Mylar fin attached to the upper surface of an airfoil at a poststall AOA.

In this paper, the experimental results reveal the generating and controlling mechanisms of the natural low-frequency oscillation. The relevant similarity parameters are considered for the aerodynamic and aeroelastic scaling of an airfoil with a flexible fin, and experiments conducted in a water tunnel are described. The results obtained from force measurements by an external balance and time-resolved velocity field measurements by particle image velocimetry (PIV) are presented. Reduction of the drag and suppression of the low-frequency oscillation in poststall flows are achieved by using a flexible fin attached to the NACA0012 airfoil model near the leading edge. Based on PIV measurements, the vortical structures developed in the shear layer and the short-time-averaged flow structures associated with the natural low-frequency oscillation in the whole

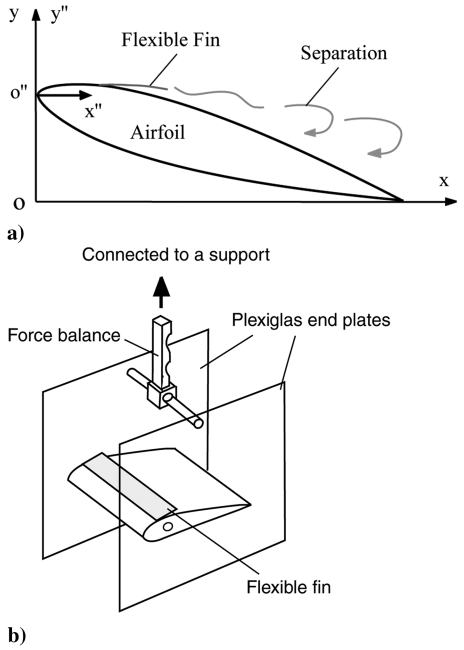

Fig. 2 Illustrations of a) concept of a thin flexible fin and coordinate systems and b) experimental setup.

separated-flow region are studied. The spectral analysis of the unsteady flowfields and the correlation analysis between the unsteady velocity field and the kinematics of fin deformation are given.

II. Similarity Parameters and Experimental Setup

The similarity parameters for a rigid airfoil with a thin flexible fin are considered. The similarity parameter for a rigid airfoil in an incompressible flow is the chord-based Reynolds number $Re_c = U_\infty c/\nu$, where U_∞ is the freestream velocity, ν is the fluid viscosity, and c is the airfoil chord. The nondimensional time parameter is $U_\infty \tau/c$, where τ is a characteristic timescale of an unsteady flow. When τ is replaced by $1/\omega$, this parameter is inversely proportional to the reduced frequency $\omega c/U_\infty$, where ω is a characteristic circular frequency of an unsteady flow.

For a flexible fin attached to the rigid airfoil, additional similarity parameters should be obtained. The flexible fin is considered as a thin cantilever plate deforming under fluid-dynamic loading. In the nondimensional differential equation for the displacement of a thin plate (e.g. fin) [32], two similarity parameters $G_1 = D_E/l^3 q_\infty$ and $G_2 = Ml/\tau^2 q_\infty$ are related to the rigidity and mass distribution of the thin plate, respectively, where D_E is the plate flexural rigidity, M is the mass distribution of the plate, $q_\infty = 0.5\rho_\infty U_\infty^2$ is the dynamic pressure, τ is a time scale, and l is the fin length. Other similarity parameters related to the damping are a_1/τ and $a_2\tau$, where a_1 and a_2 are constant damping coefficients in the damping operator in the equation for a thin plate. Therefore, the functional relation for a force coefficient C_F of an airfoil to which a flexible fin is attached at a fixed position can be generally expressed by $C_F = f(\alpha, Re_\infty, G_1, G_2, a_1/\tau, a_2\tau)$. In this study, the effects of AOA are mainly considered at a fixed Reynolds number. Since a Mylar fin with the fixed length and thickness is used, the nondimensional parameters related to the fin are fixed. In the future, further study should be done in the whole parametric space.

Experiments were conducted in a water tunnel (Rolling Hills Research Corporation model 1520) in the Fluid Mechanics Laboratory at Western Michigan University. The glass test section is nominally 381 mm wide, 508 mm high, and 1524 mm long. The tempered glasses, which are 9.5 mm thick on the sidewalls and 12.7 mm thick on the bottom, are mounted with silicon rubber, allowing good optical access from the top, bottom, both sides, and rear for flow visualization and PIV measurements. The tunnel is operated as a continuous-flow channel and the water level in the test section is typically adjusted to be roughly 50 mm below the top of the walls. The free water surface provides simple access to the model and easy setup of an external force balance. There is a 6:1 contraction section upstream of the test section for turbulence reduction and avoidance of local separation and vorticity development. The test section flow velocity can be adjusted, and the maximum velocity is 0.3 m/s. In the test section, the turbulence intensity is less than 0.1%. The velocity nonuniformity is less than 2%. The mean flow angularity is less than 0.01° in both the pitch and yaw directions.

Figure 2b is a schematic view of the experimental setup. A resin NACA0012 airfoil model built by a rapid-prototype machine was tested. The chord and span of the model were 254 and 304.8 mm, respectively. A rectangular clear Mylar (PET-polyester) film with a thickness of 0.1 mm was used as a flexible fin. The width of a film was the same as the airfoil section span. After several films with different lengths were tested, a Mylar film with a length of 25% chord (63.5 mm) was selected as a typical fin for a systematic study. Young's modulus and Poisson's ratio for Mylar were 2.8 GPa and 0.37, respectively. The 18-mm-long section of one end of an 81.5-mm-long rectangular Mylar film was fixed to the upper surface of the airfoil by a double-stick Scotch tape, and then the top of the film in that portion was reinforced by a single-stick Scotch tap. This sandwich structure ensued that the clamped end of the film was tangent to the airfoil surface at the root of the fin. The cantilever portion of the fin was 63.5 mm (25%c).

To reduce the three-dimensionality of the flow, the model was mounted between two 6.35-mm-thick Plexiglas end plates (406 by

279 mm) that were supported by an aluminum bar. The bar was directly connected to an external force balance that was above the water surface. In spite of the existence of the finite end plates, the NACA0012 airfoil model should be considered as a finite rectangular wing that is more like a low-aspect-ratio (AR) rectangular wing with very large plate winglets. It will be pointed out later that a fit to the lift data of the baseline model by using the to the McCormick's formula gives the effective AR AR $= 4.42$ that is larger than the physical aspect ratio of 1.2. The end plates substantially reduced the three-dimensionality of flow. Although the finite end plates do not completely eliminate the three-dimensionality of flow, they modify the tip vortices acting like large winglets. The blockage of the model at AOA $= 18°$ in the water tunnel is about 13%. Although the effect of the blockage is not directly evaluated, the lift coefficient as a function AOA obtained in the water tunnel is in agreement with that obtained for the same model with a much smaller blockage (about 2%) in a large wind tunnel [33]. This indicates that the blockage of the model did not change the lift characteristics.

For measurements of very small drag force, the main balance element was a 275-mm-long aluminum beam with a 30-mm-thick and 12.75-mm-wide cross section. Two sections of the beam were machined and considerably thinned, and the center locations of the two thinned sections were at 6.4 and 11.3 mm from the corresponding end. The thickness and length of the thinned sections are 2.75 and 35 mm, respectively. Two Omega strain gauges were installed at the middle of the thinned sections. When the balance element (beam) was mounted perpendicularly to the incoming flow direction, the difference between voltage outputs from the two strain gauges simply equaled to a product of the drag and the distance between the two gauges. Balance calibrations verified this simple and direct relationship. The measurement uncertainty of drag was less than 1 g. A similar beam was used for lift measurement when this beam was parallel to the incoming flow direction. The frequency response of the balance element was detected in impulse tests, where impulse forcing was provided by a hammer hitting on the element. The deformation of the beam element was measured by a video-grammetric system at 42 frames/second, and the power spectra of the beam deformation were obtained. The natural frequencies of the element were found at 6 and 12 Hz, which were associated with the two thinned sections of the element. In our experiments, the low-frequency mode measured by the balance was at about 0.1 Hz, which was much smaller than 6 Hz. Therefore, according to the frequency-response curve, the balance was sufficient to resolve the fluctuations of the drag and lift, and steady-state calibration result could be used for quasi-unsteady measurements.

The flow around the model was illuminated by a 2-mm-thick laser sheet generated by a Big Sky laser (CFR190) entering from the rear window of the test section. The laser frequency was set at 15 Hz, which was sufficient for time-resolved measurements in this study, since the dominant frequencies of the flows were lower than 0.5 Hz. The interval between two laser pulses was 2 ms. The measuring area was imaged by a PIV camera (TSI PIVCAM 10-30, model 630046) with an 85 mm lens. PIV images were processed using the TSI Insight5 PIV software. The interrogation window size is 32×32 pixels in a 1000×1000 pixels image, which corresponds to an 8×8 mm area in a laser sheet illuminating the whole cross section of the airfoil model. There are about 28 particles in an interrogation window, which can achieve good correlation calculations. The accuracy of the TSI PIV system has been examined in comparison with other commercial and research systems [34]. In this work, PIV measurements were evaluated by measuring the uniform flow velocities in the water tunnel without a model. It is found that the difference between the velocities given by PIV and flow rate measurement is about 3%.

III. Flow Control Using Passive Flexible Fin

A. Drag Reduction and Oscillation Suppression

A rectangular Mylar fin with a thickness h of 0.1 mm and a length l of $0.25c$ (63.5 mm) was first used in preliminary tests, where the airfoil chord c is 254 mm. The incoming flow velocity was 0.25 m/s, and the chord-based Reynolds number was $Re_c = 6.3 \times 10^4$. The similarity parameter for the flexural rigidity of the fin is $G_1 = D_E/l^3 q_\infty \approx 338$, where $D_E = Eh^2/12(1-\nu^2)$ is the flexural rigidity, Young's modulus E is 2.8 GPa, and Poisson's ratio ν is 0.37. To examine how a flexible fin affects the drag of the airfoil, the fin was placed at different locations on the upper surface of the NACA0012 airfoil model. In addition, two tandem fins at different locations were tested. All the configurations can achieve a reduction of the drag in poststall flows. The effects of the length of a flexible fin are also examined. It is found that a longer fin can suppress the low-frequency oscillation more effectively at a cost of increasing the skin-friction drag on the fin. Therefore, a fin with the length of $0.25c$ is selected as a suitable medium-size fin for systematic tests. Throughout the paper, the fin is the $0.25c$ fin.

Figure 3a shows the time-averaged drag coefficient C_D as function of AOA for different arrangements of the flexible Mylar fins. For flows at AOA smaller than 12°, it has been observed that a flexible fin on the model was naturally buoyant in water, causing the increased drag compared with that of the baseline model. This problem could be practically resolved by somehow making the flexible Mylar fin attached on the surface for small AOA before stall. In fact, measurements indicated that the model with a fin fully attached on the surface by Scotch tape was approximately equivalent to the

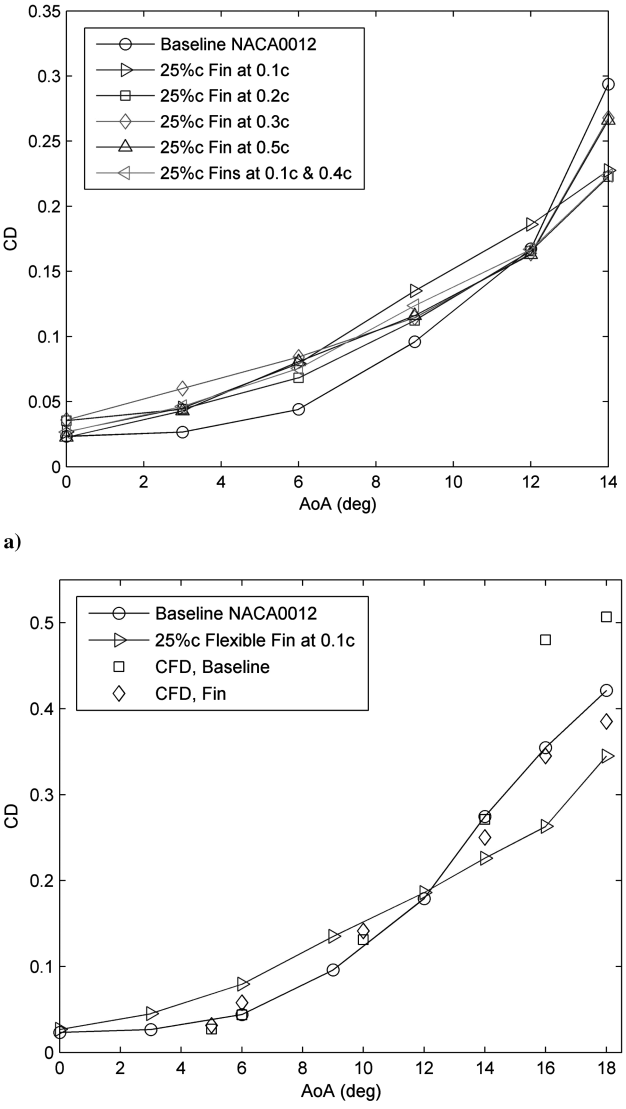

Fig. 3 Drag coefficient as a function of AOA for a) different fin arrangements and b) the $0.25c$ fin located at $0.1c$ at the chord-based Reynolds number $Re_c = 6.3 \times 10^4$.

baseline model in terms of the aerodynamic characteristics. When AOA is larger than 12°, C_D of the NACA0012 airfoil model with a flexible fin is smaller than that of the baseline model. As will be shown in Sec. IV, a flexible fin passively alters the flow structures to suppress the revered flow and reduce the drag at high AOA. As a typical case for detailed investigations, a significant drag reduction at high AOA by the fin located at $0.1c$ is shown in Fig. 3b. The absolute measurement uncertainty of drag is 1 g, and the relative uncertainty of C_D is 1–3% in a range of AOA from 12 to 20°.

The computational fluid dynamics (CFD) results of the drag coefficient for the same case are also given in Fig. 3b, which are obtained by using an unsteady Reynolds-Averaged Navier–Stokes (RANS) solver combined with the immersed boundary method (IBM) coupled with a finite element structure code for turbulent flows [35]. The CFD prediction is roughly consistent with the measured results, particularly indicating a drag reduction although the CFD drag values are considerably larger when AOA is larger than 12°. Although the unsteady RANS code cannot provide the fully-time-resolved flowfields with high spatial resolutions for detailed comparison of the development of vortical structures with global velocity measurements, the time-averaged CFD results still provide useful information in addition to the experimental data. CFD calculations indicate that the pressure drag is considerably reduced by the fin at high AOA. The skin-friction drag is increased for small AOA as the fin is detached from the surface in the calculations.

Figure 4 shows the lift coefficient as a function of AOA for the baseline model and model with the fin. The data obtained in the wind-tunnel testing at $Re_c = 4.74 \times 10^5$ [33] are also shown in Fig. 4 for reference. Note that the lift coefficient of the model with the fin in the nonstalled flow for AOA < 15° is the same as that of the baseline model when the whole fin is attached to surface by Scotch tape. According to the McCormick's formula [33], the lift slope depends on the AR by

$$a = \frac{\mathrm{d}C_L}{\mathrm{d}\alpha} = \frac{a_0 \mathrm{AR}}{\mathrm{AR} + 2(\mathrm{AR}+4)/(\mathrm{AR}+2)}$$

where $a_0 = 2\pi$ according to thin airfoil theory. As shown in Fig. 4, a fit by using McCormick's correlation formula for the wind-tunnel data gives the effective AR of 4.42. It is emphasized again that the airfoil model used in this study is not 2-D and it should be treated as a finite rectangular wing. The downwash induced by the tip vortices of the baseline model is significant even though the two finite end plates are used to reduce the three-dimensionality of flow. According to the lifting-line theory, the induced AOA when stall occurs is $\alpha_i = C_L/\pi\mathrm{AR} \approx 4°$, where the effective AR is 4.42. As shown in Fig. 4, the geometrical AOA at the maximum lift coefficient for the baseline model is about 15°, and the corresponding effective stalled AOA is about 11°. In general, the geometrical AOA is referred to as AOA in this paper. It is noted that the lift of the model with a flexible fin is decreased in poststall flows at high AOA (greater than 14°). It will be pointed out later that the lift loss is mainly caused by suppression of the lift-generating organized vortical structures in the separated shear layer by the fin, which is also responsible to the reduction of the drag and suppression of the low-frequency oscillation in poststall flows. This is opposite to the vortex-induced lift enhancement by unsteady forcing near the leading edge found by

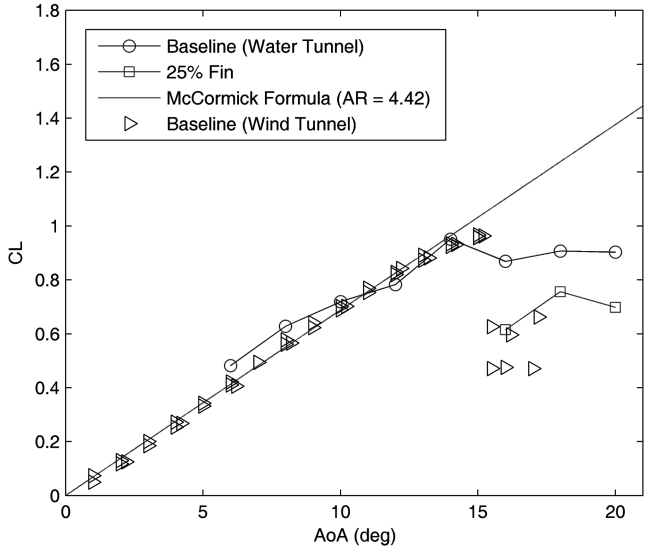

Fig. 4 Measured lift coefficient of the NACA0012 airfoil model as a function of AOA.

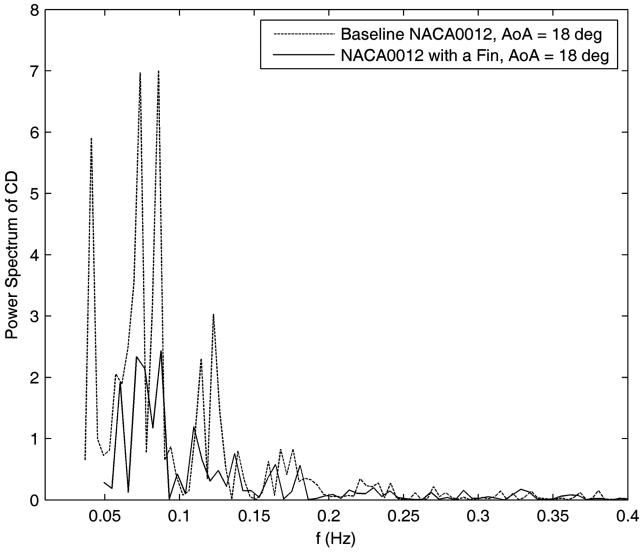

Fig. 5 Power spectra of the drag coefficient for the baseline NACA0012 airfoil model and model with the fin located at $0.1c$ at AOA of 18°.

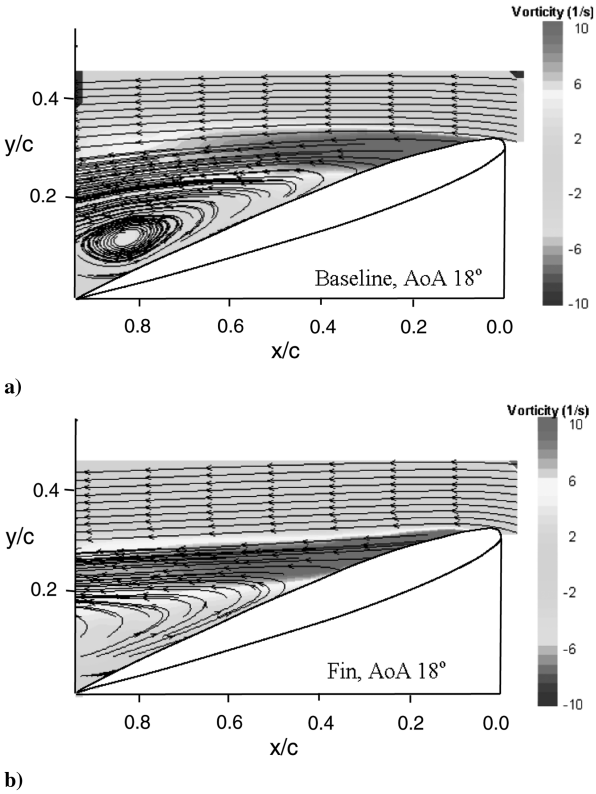

Fig. 6 Time-averaged streamlines and vorticity distributions for a) the baseline NACA0012 airfoil model and b) model with the fin located at $0.1c$ at AOA of 18°.

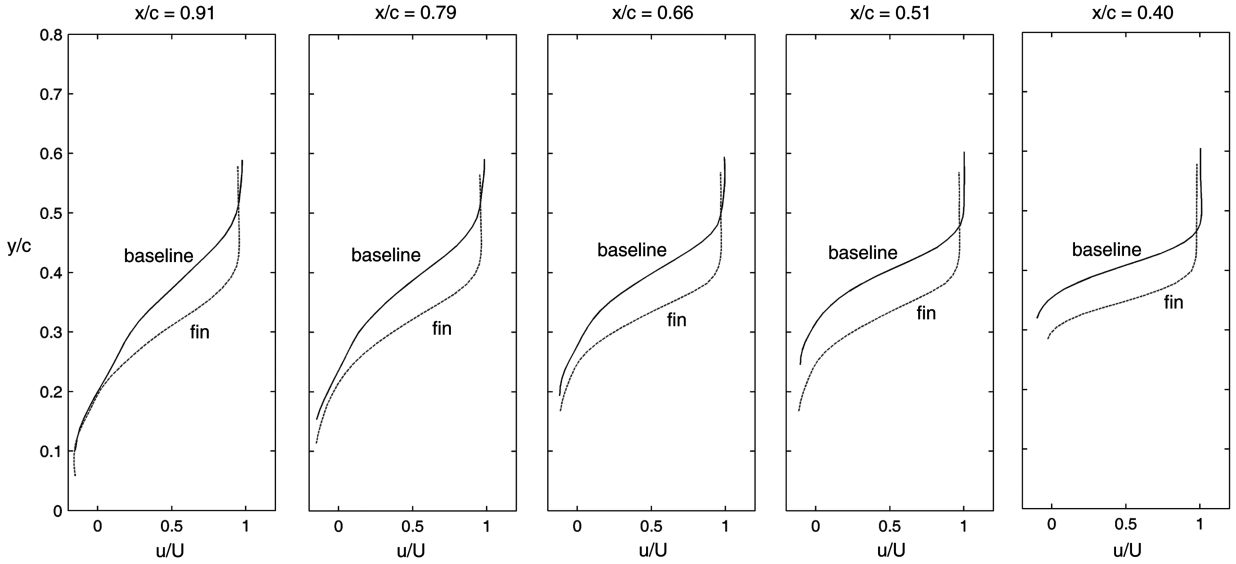

Fig. 7 Profiles of the mean velocity component $\langle U \rangle$ at different x locations on the upper surface for AoA = 18°.

Wu et al. [21]. Therefore, the lift loss in poststall flows is considered as a side effect of a flexible fin. Further discussions will be given based on detailed measurements of flow structures.

Naturally, the drag of the NACA0012 airfoil model varies with time due to the highly unsteady nature of poststall flows. The root-mean-squared variation of the drag coefficient C_D of the baseline model is about 3% of the mean value. The power spectra of C_D are shown in Fig. 5 for the baseline model and the model with the flexible fin at AOA of 18°. The spectral peaks at 0.04, 0.07, and 0.08 Hz correspond to $St_{\mathrm{LF}} = 0.012$, 0.022 and 0.025, respectively. These low-frequency fluctuations of the drag are basically corresponding to the natural low-frequency oscillation studied by Zaman et al. [15]. Similar low-frequency components were also found at AOA of 14, 16, and 20°. In our experiments, the baseline model swung as a pendulum relative to the support at a low frequency (see Fig. 2b for the structure), which was observed in a range of AOA from 14 to 20°. Interestingly, as indicated in Fig. 5, the low-frequency drag fluctuations, along with the visible model swing, are considerably dampened by the flexible fin attached at $0.1c$. In the following, the physical mechanisms of the reduction of the drag and suppression of the low-frequency oscillation will be explored based on time-revolved PIV measurements of flowfields.

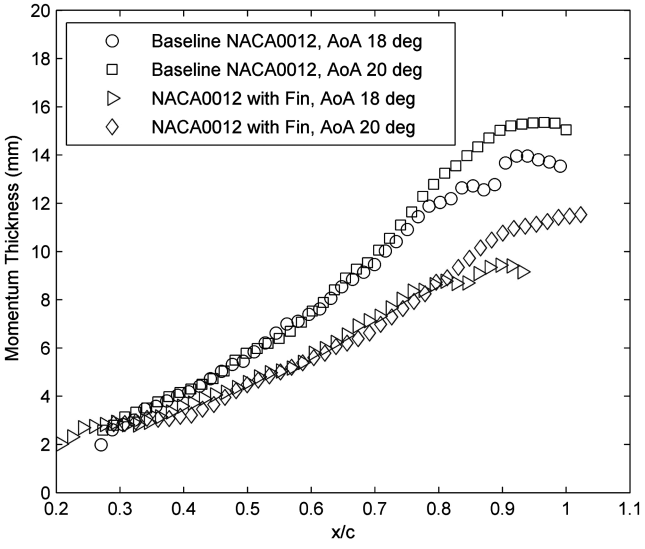

Fig. 8 Effect of the flexible fin on the development of the momentum thickness in the separated-flow region.

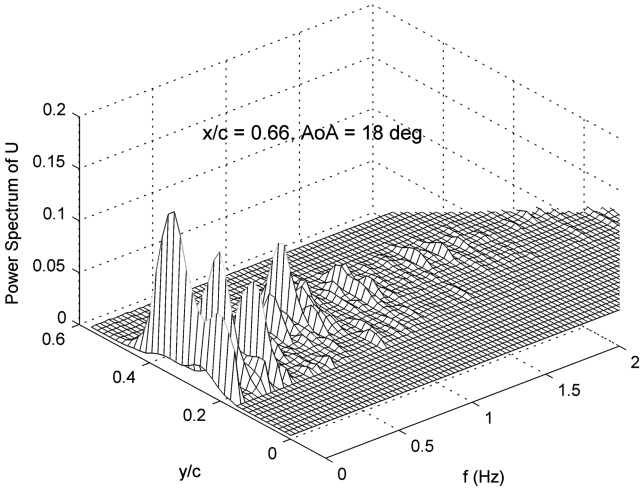

a)

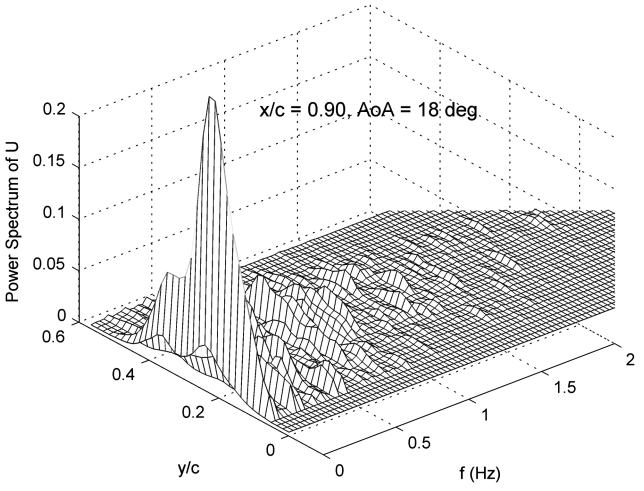

b)

Fig. 9 Power spectra of the velocity component U across the separated-flow region at two x locations for the baseline NACA0012 airfoil model at AOA of 18°.

B. Development of Flow Structures

1. Mean Flow Properties

To understand the physical mechanisms of the drag reduction by a flexible fin, PIV measurements of the flowfields were conducted and velocity fields were obtained at 15 Hz. Figure 6 shows the time-averaged streamlines and vorticity fields for the baseline model and the model with the fin located at $0.1c$ at AOA of 18°. The change of the velocity fields generated by the flexible fin is appreciable. For the baseline model, a time-averaged large recirculating flow region is observed on the upper surface near the trailing edge of the airfoil, which can be loosely considered as an open separation bubble in a long-time-average sense. Indeed, a time sequence of velocity and vorticity fields indicates that strong large-scale organized vortical structures are developed from the Kelvin–Helmholtz (K-H) instability in the separated shear layer. Although the evolution process of these vortical structures is highly unsteady, they occur intermittently at a higher probability in that region, inducing the strong reversed flow. In contrast, due to the presence of the flexible fin, the time-averaged large recirculating flow is considerably weakened and shifted downstream.

Figure 7 shows the profiles of the x component of the mean velocity $\langle U \rangle$ at $x/c = 0.4$, 0.51, 0.66, 0.79, and 0.91 on the upper surface for AOA of 18°, where x is the coordinate along the incoming flow direction from the leading edge. Clearly, the momentum loss is reduced in the separated-flow region due to the presence of a flexible fin, which corresponds to the drag reduction found in the force measurements by the external force balance. Further evidence is provided by the momentum thickness development along the x direction, as shown in Fig. 8. Here, the momentum thickness across the separated flow is defined as

$$\theta = \int_{y_s}^{\infty} \frac{\Delta U(y)}{\Delta U_e}\left[1 - \frac{\Delta U(y)}{\Delta U_e}\right] \mathrm{d}y$$

where $\Delta U = \langle U \rangle - \min(\langle U \rangle)$, $\Delta U_e = U_e - \min(\langle U \rangle)$, $\langle U \rangle$ is the x component of the mean velocity, U_e is the external velocity, and y_s is the y coordinate at the upper surface. As indicated in Fig. 8, the increasing rate of the momentum thickness along the main streamwise direction is significantly reduced by the flexible fin.

2. Unsteady Flow Properties

Figure 9 shows typical power spectra of the x component of velocity U along the y direction at $x/c = 0.66$ and 0.90 across the separated-flow region for the baseline model at AOA of 18°, and Fig. 10 shows those for the model with the fin located at $0.1c$. The spectra were calculated from a total of 2500 instantaneous velocity fields (sampled at 15 Hz over an interval of 167 s). The coordinate

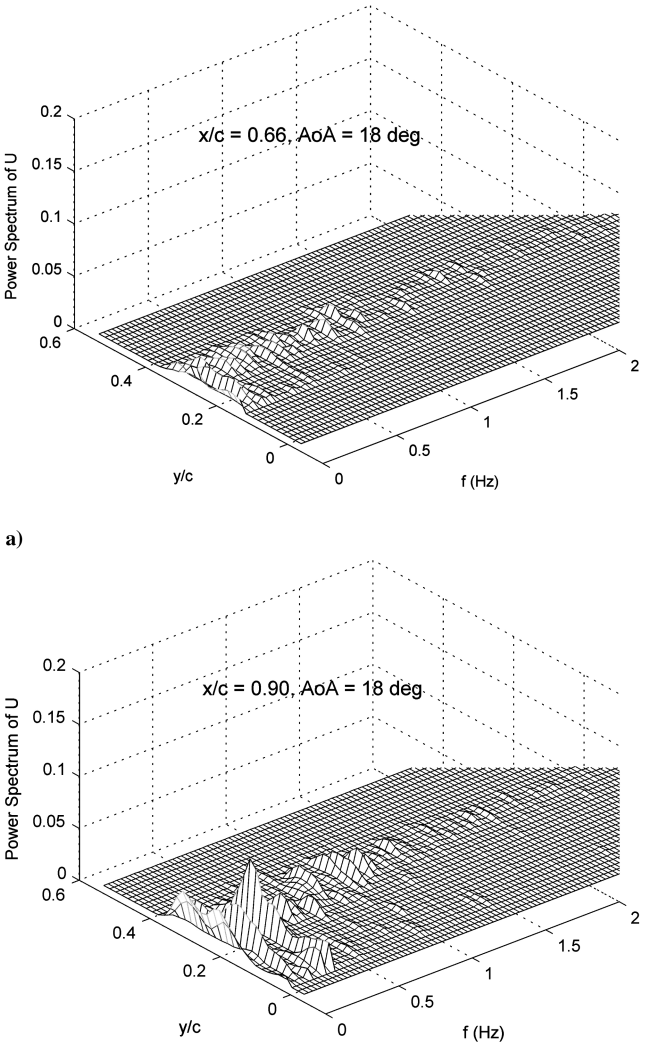

Fig. 10 Power spectra of the velocity component U across the separated-flow region at two x locations for the NACA0012 airfoil model with the flexible fin located at $0.1c$ at AOA of 18°.

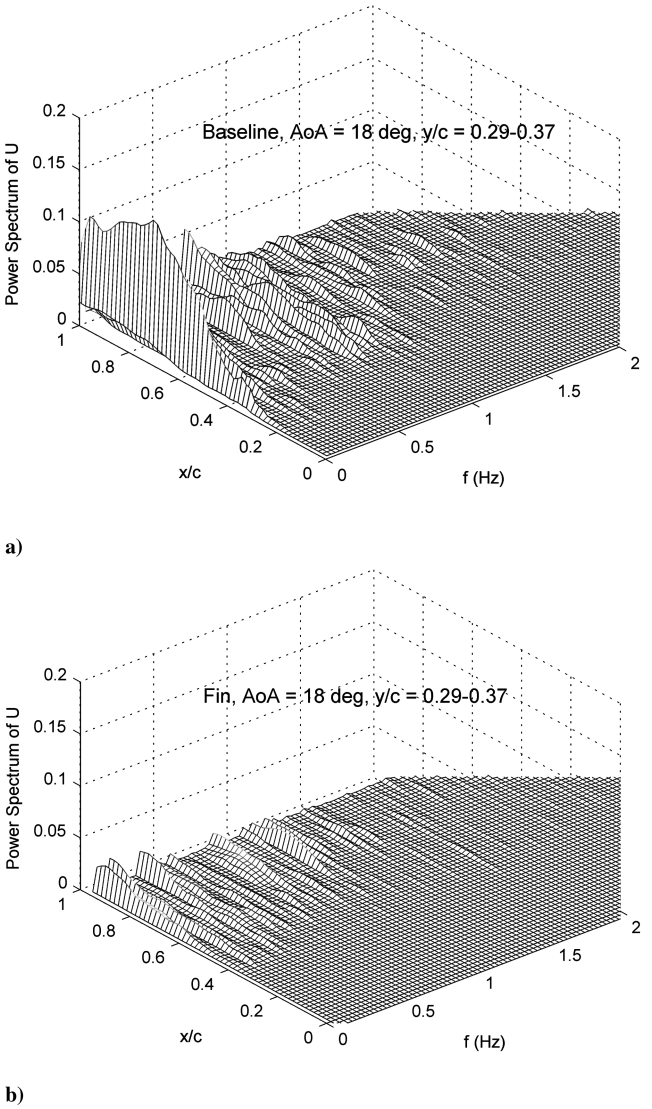

Fig. 11 Development of spectral components of the velocity component U across the shear layer in the x direction at AOA of 18° for a) the baseline NACA0012 airfoil model and b) model with the flexible fin located at $0.1c$.

system (x, y) is illustrated in Fig. 2a. For the baseline model, the dominant spectral component at $f = 0.07$ Hz is developed downstream. The Strouhal number of this low-frequency component based on the initial shear-layer momentum thickness is $St = f\theta_0/U_e = 8.4 \times 10^{-4}$, where $\theta_0 = 2$ mm is the estimated initial momentum thickness at $x/c = 0.2$ (see Fig. 8). Since this Strouhal number is much smaller than the most unstable mode ($St_{\text{shear}} = 0.032$) in the shear layer, therefore, the low-frequency component is unlikely to be directly related to the shear-layer mode associated with the linear shear-layer instability. In fact, the Strouhal number based on the front-projected chord $c\sin(\alpha)$ is $St_{\text{LF}} = fc\sin(\alpha)/U_e = 0.022$, which is consistent with the natural low-frequency oscillation [15]. This low-frequency component of the velocity U is responsible to the fluctuation of the drag coefficient shown in Fig. 5. Figure 10 shows the effect of a flexible fin on the power spectra of U, indicating that the dominant low-frequency component and other components of U are significantly suppressed. This is also consistent with the measurements of the drag, as shown in Fig. 5.

Furthermore, Fig. 11 shows the development of the spectral components averaged across the separated shear layer ($y/c = 0.29$–0.37) along the x direction for the baseline model and the model with the fin located at $0.1c$. For the baseline model, the dominant low-frequency component at $f = 0.07$ Hz ($St_{\text{LF}} = 0.022$) is amplified in a nearly linear fashion in $x/c = 0.2$–0.8, and then it saturates and decays. As indicated in Fig. 11b, the development of all the spectral components particularly the dominant low-frequency component at $f = 0.07$ Hz ($St_{\text{LF}} = 0.022$) is suppressed by the flexible fin.

IV. Shear-Layer Vortical Structures and Low-Frequency Oscillation

The above results indicate that a flexible fin dramatically dampens the dominant spectral components, particularly the low-frequency oscillation, in the separated-flow region over the NACA0012 airfoil model. To understand the underlying mechanisms, it is necessary to examine the development of vortical structures in the separated shear layer and the generation of the low-frequency oscillation on the baseline NACA0012 airfoil model. Figure 12 shows the streamlines and vorticity fields, indicating energetic vortical structures developed in the shear layer from the leading edge of the baseline model in an interval of 1.0 s. The vorticity sheet in the shear layer rolls up into a discrete vortical structure due to the K-H instability and shed from the leading edge. The vortical structure travels downstream as their size increases, and another vortical structure remains observable near the

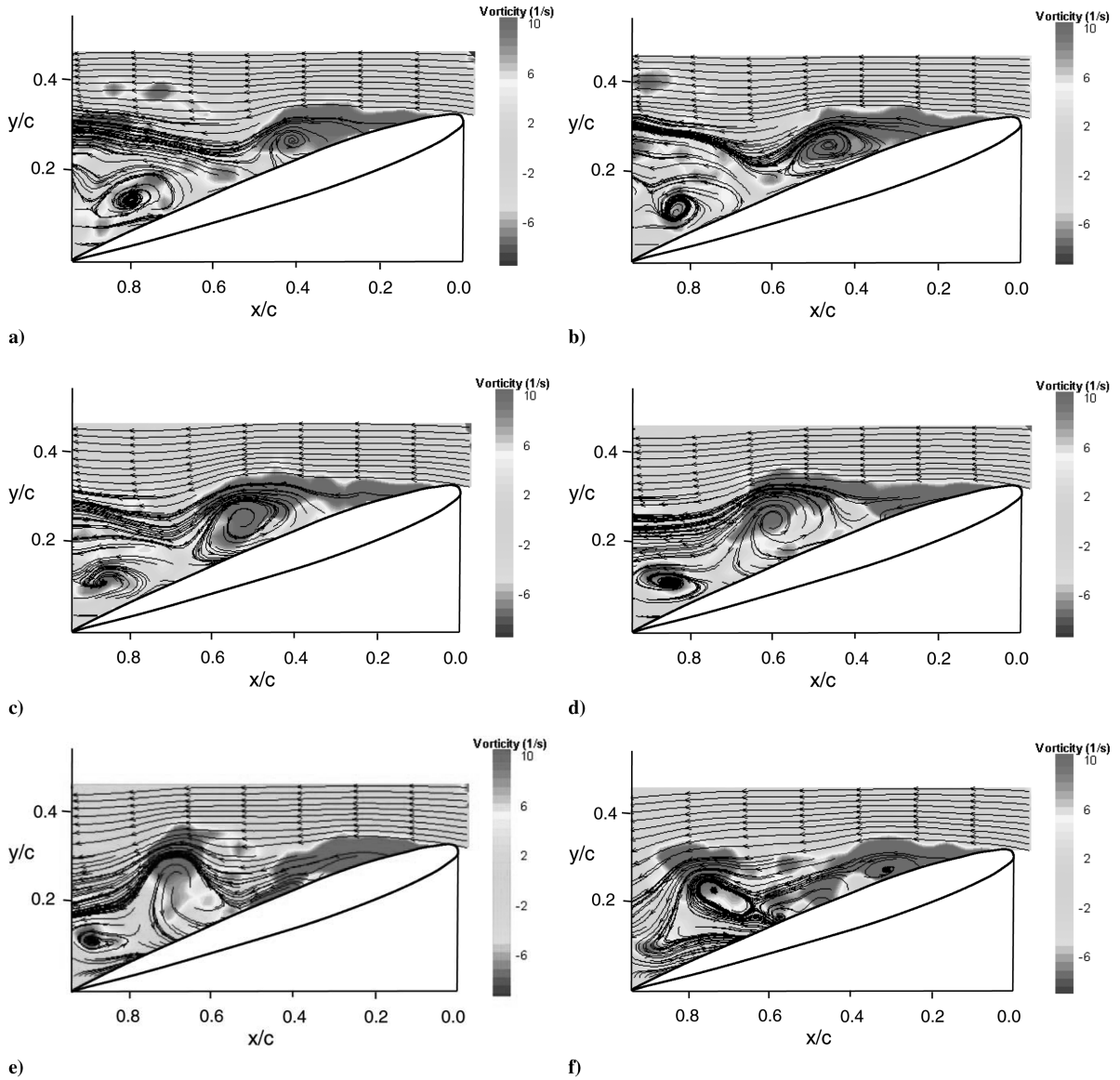

Fig. 12 Snapshot velocity fields of vortical structures developed in the shear layer from the leading edge for AoA = 18° at a) 0 s, b) 0.2 s, c) 0.4 s, d) 0.6 s, e) 0.8 s, and f) 1.0 s.

trailing edge. The dual-vortex structure on the upper surface of the model is typically observed as shown in Figs. 12a–12c, and this structure is similar to that observed in dynamic stall [36]. Then, the two vortical structures intermittently merge to form a larger stronger vortical structure inducing strong reversed flow near the trailing edge. The vortical structures developed in the separated shear layer shed at about 1 Hz in this case, and the corresponding Strouhal number St_θ based on the median momentum thickness (8 mm) in the shear layer is about 0.032 that correspond to the most unstable mode in the shear layer. Interestingly, when the front-projected chord rather than the momentum thickness is used as a length scale, the Strouhal number is $St = fc\sin(\alpha)/U_e = 0.31$, which is close to the bluff-body vortex-shedding Strouhal number. This correspondence between the K-H instability in the shear layer and the vortex-shedding mode may be coincident for the poststall airfoil flow at a suitable AOA. In general, for a bluff body like a circular cylinder, the shear-layer mode is very different from the bluff-body vortex-shedding mode.

PIV measurements were conducted to focus on the region near the leading edge. Figure 13 shows the power spectra of the velocity components U and V at $0.45c$ for the baseline model. In Fig. 13, a local coordinate system (x'', y'') located at the leading edge is used for convenience as shown in Fig. 2a. The translation transformations between the coordinate systems (x, y) and (x'', y'') are $x'' = x$ and $y'' = y - c\sin\alpha$. Interestingly, the dominant spectral peak at 1 Hz, which is the shear-layer mode, appears in the spectrum of the normal

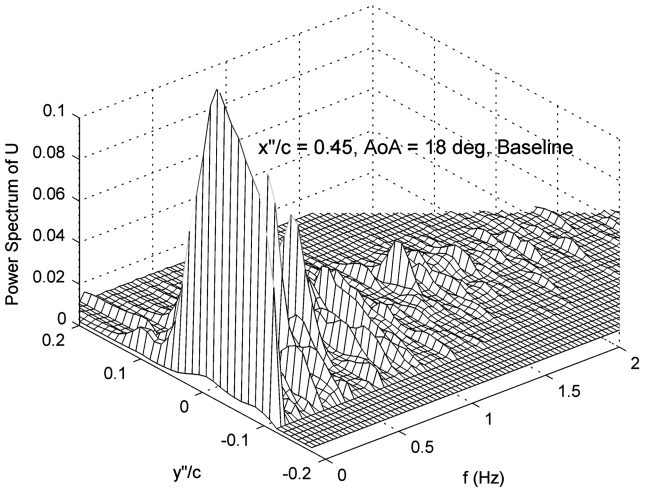

a)

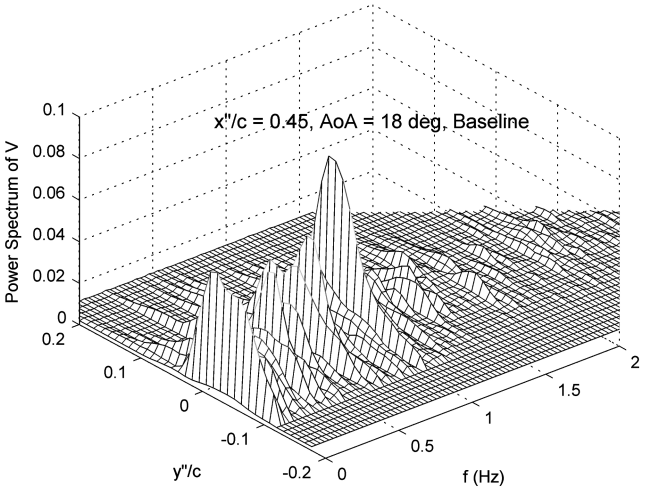

b)

Fig. 13 Power spectra of the velocity components at $x''/c = 0.45$ for the baseline NACA0012 airfoil model: a) U and b) V.

velocity V. In contrast, the dominant component in the spectrum of U is at 0.07 Hz that corresponds to the natural low-frequency oscillation at $St_{\mathrm{LF}} = 0.022$. The low-frequency mode in the spectra of U is detected in the whole separated-flow region. In the spectra of V, the shear-layer mode is strong in 0.3–$0.5c$, and the low-frequency mode becomes more evident near the trailing edge. This indicates that the low-frequency oscillation is a global phenomenon, and in contrast the vortical structures developed in the shear layer are more active near the leading edge. These two salient modes coexist in poststall flows over the NACA0012 airfoil model. Although the Strouhal number of the shear-layer mode increases with x/c due to the increased momentum thickness, the median value of St_θ is about 0.032 that is the most unstable mode in the shear layer. This provides a connection between the vortical structures developed from the leading edge and the shear-layer instability. On the other hand, compared with the most unstable mode in the shear layer, the Strouhal number for the low-frequency mode is so small that any direct relationship between the low-frequency oscillation and the K-H instability is excluded.

Zaman et al. [15] suggested that the natural low-frequency oscillation might be attributed to intermittent switching between stalled and unstalled flows. Phase-averaged flowfield measurements by Broeren and Bragg [18] found that the generation and growth of a separation bubble from the leading edge and its merging to the trailing-edge separation could cause the low-frequency oscillation. However, due to the highly unsteady flows with a considerable degree of randomness in PIV measurements, the scenario of a steadily growing bubble near the leading edge described by Broeren and Bragg [18] has not been clearly observed in this case. To gain insight into the origin of the low-frequency oscillation, the center of the large-scale recirculating flow in the time-averaged velocity field in Fig. 6a is selected as a reference point for an analysis of the temporal signal of U. In fact, this reference point is the mean zero-crossing point of U. There is an instantaneous zero-crossing point across which U changes its sign, which characterizes the instantaneous boundary of the reversed flow. Figure 14 shows the time traces of the velocity U and the zero-crossing point position at the reference point. The zero-crossing point is detected from the instantaneous U-velocity profiles along the y coordinate at the reference point. Although there is a considerable amount of higher-frequency components, the low-frequency oscillation of about 0.1 Hz is visible, and the power spectra clearly show the dominant peak at about 0.1 Hz for both the velocity U and the zero-crossing point position.

By comparing Fig. 14a with Fig. 14b, it is found that the positive peaks of the velocity U correspond to the valleys of the zero-crossing point position at the reference point. Similarly, the negative valleys of U correspond to the peaks of the zero-crossing point position. The mean phase difference between U and the zero-crossing point position over a frequency range of 0.05–0.5 Hz is 174°. This clearly indicates the relationship between the local velocity U and the boundary of the reversed flow at the reference point. Further, the magnitude-squared coherence between the velocity U and the zero-crossing point position y_{cp} is calculated, i.e.,

$$C_{y_{\mathrm{cp}}U} = \frac{|P_{y_{\mathrm{cp}}U}(f)|^2}{P_{y_{\mathrm{cp}}y_{\mathrm{cp}}}(f)P_{UU}(f)}$$

where $P_{y_{\mathrm{cp}}U}(f)$ is the cross power spectral density, and $P_{y_{\mathrm{cp}}y_{\mathrm{cp}}}(f)$ and $P_{UU}(f)$ are the power spectral densities. $C_{y_{\mathrm{cp}}U}$ is a function of frequency with values between 0 and 1 that indicates how well y_{cp} corresponds to U at each frequency. Figure 15 shows the magnitude-squared coherence $C_{y_{\mathrm{cp}}U}$, which indicates a high correlation value of 0.9 between the velocity U and the zero-crossing point position y_{cp} at 0.07 Hz (another dominant peak is at 0.45 Hz). The above results show that the low-frequency oscillation is correlated with the fluctuation of the zero-crossing point position. In other words, the low-frequency oscillation corresponds to the fluctuation of the boundary of the reversed flow.

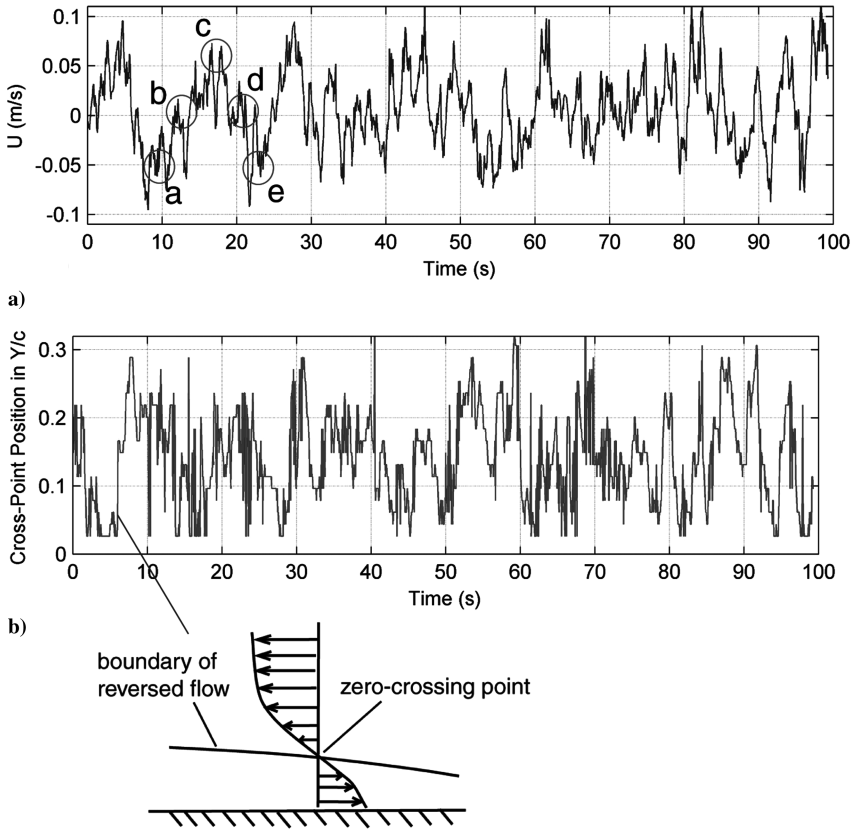

Fig. 14 Plots of a) time traces of the velocity U and b) zero-crossing point position at the reference point, where the circles mark the phases for further examination of the short-time-averaged velocity fields.

Further, it is required to extract the flow structures associated with the low-frequency oscillation from the instantaneous velocity fields that also contain the active development of the vortical structures in the separated shear layer at a much higher frequency. To filter out the velocity components associated with the shear-layer mode in the instantaneous flowfields, the velocity fields are averaged over a period of the shear-layer mode (a relatively short time interval of 0.73 s) at five selected phases in a low-frequency cycle of U (about 12 s). These phases are marked by open circles on the time trace of U at the reference point in Fig. 14a. The short-time-averaged velocity fields at the five phases are shown in Fig. 16, which reveal the hidden flow structures associated with the low-frequency oscillation. As shown in Fig. 16a, at the valley in U at the reference point, the strong recirculating flow is observed in a sense of the short time average, which is induced by the occurrence of strong vortical structures developed in the shear layer. Figure 16a also indicates that a smaller vortical structure forms near the leading edge. As shown in Fig. 16b, the newly formed vortical structure grows as it travels downstream. In Fig. 16c, at the peak of U at the reference point, the velocity of the reversed flow becomes much smaller, since the strong vortical structures are gone at that moment, and the topological structure of streamlines is considerably different. Figures 16d and 16e indicate that the large vortical structures occur and develop again. The low-frequency oscillation is related to periodic switching between the larger strong and smaller weak recirculating flows induced by the vortical structures in the separated shear layer. This is consistent with the above analysis of the zero-crossing point position. This scenario is different from the mechanism proposed by Broeren and Bragg [18] based on interaction between the leading-edge separation bubble and trailing-edge separation. In our experiments, a closed separation bubble near the leading edge was not observed, and the separated flows were open.

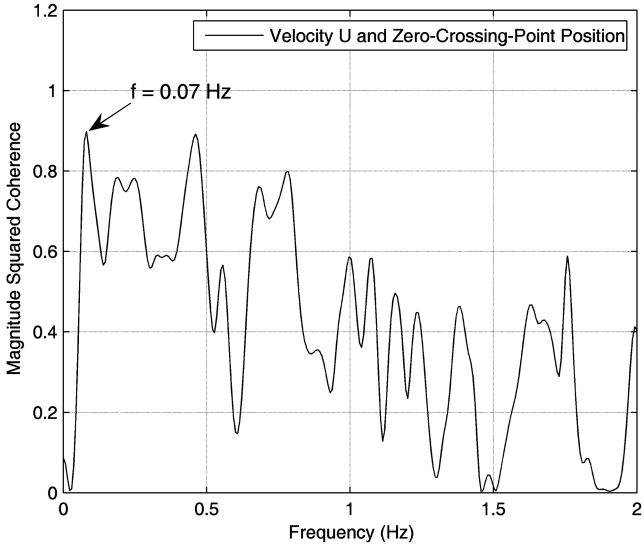

Fig. 15 Magnitude-squared coherence between the velocity U and the zero-crossing point position at the reference point.

In summary, a flexible fin attached to the upper surface near the leading edge suppresses the large vortical structures in the shear layer and consequently the low-frequency oscillation. Clearly, a negative consequence of such suppression is a loss of the lift induced by these vortical structures in poststall flows, which is indicated in Fig. 4. The increased lift induced by a vortex or several vortices traveling through the upper surface of an airfoil is explained by the theoretical models [37,38] and the numerical simulations [21]. Also, it is noted that increased lift can be obtained by using movable flaps near the trailing edge as dams blocking the reversed flow near stall for certain thick airfoils [28–30]. A flexible fin near the leading edge used here passively manipulates the flow structures in the shear layer and affects the whole separated-flow region, resulting in suppression of the low-frequency oscillation and

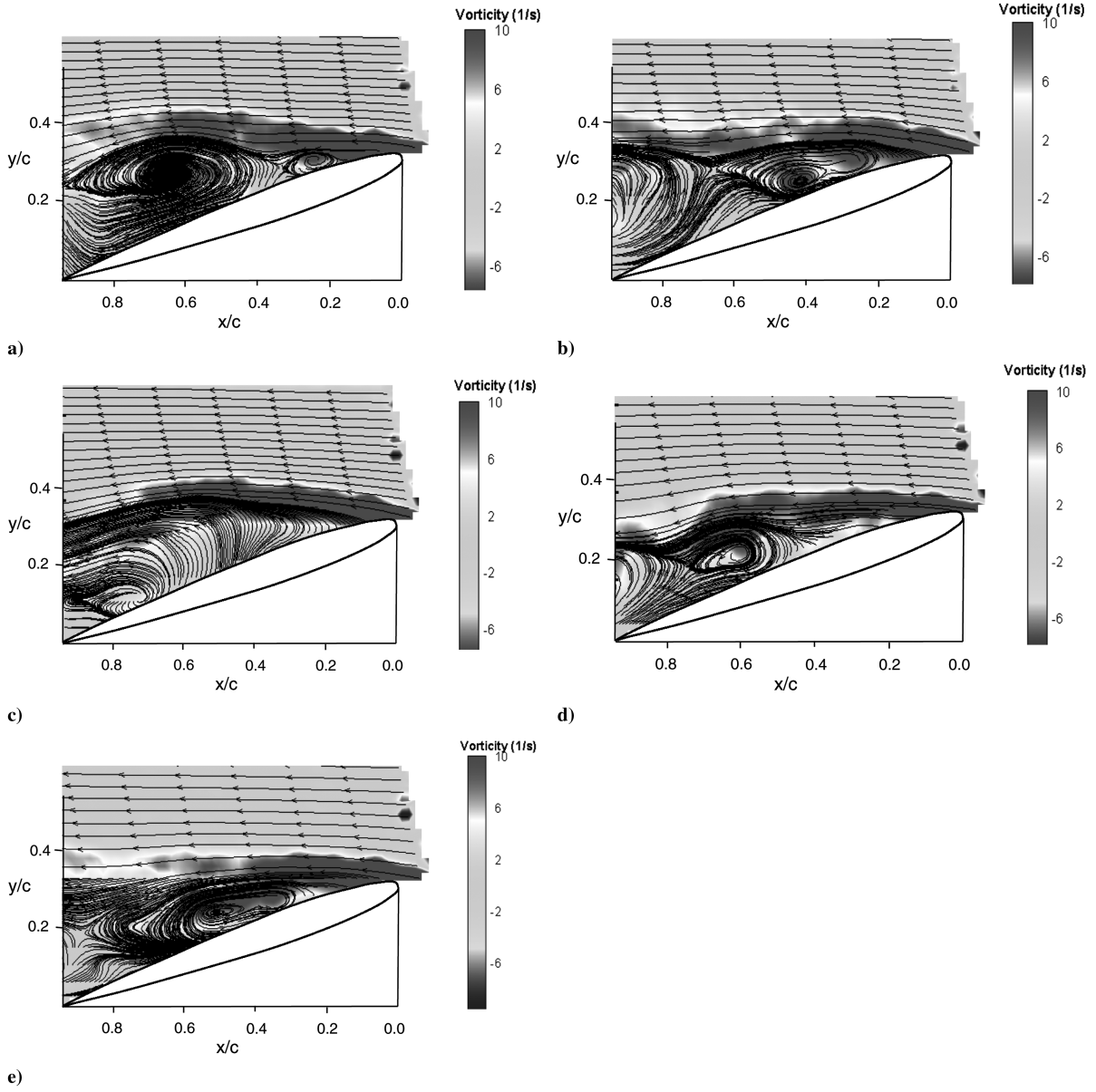

Fig. 16 Velocity fields averaged over a period of the shear-layer mode (a short period of 0.73 s) at the five phases indicated in Fig. 14a in a low-frequency cycle of the reference velocity U (about 12 s): a) the first valley, b) the first middle point between the peak and valley, c) peak, d) the second middle point, and e) the second valley.

reduction of the drag. Potentially, a combination of a flexible fin near the leading edge and a movable flap near the trailing edge could be used in near-stall and poststall flows.

V. Interaction Between Flexible Fin and Unsteady Flow

To understand the interaction between a flexible fin and the surrounding unsteady flow, it is necessary to measure the kinematics of fin deformation and the unsteady flow near the fin from PIV. The fin is clearly visualized in PIV images as an intersection between the fin and laser sheet. The high-contrast edges of the fin in images are detected by using the Canny's edge detector. The coordinates of the fin edges are fitted by using the characteristic beam functions for dynamic deformation of a rectangular plate [39] and then the magnitude of fin deformation is determined as a function of time.

In our experiments, the deformation of a flexible fin was nearly 2-D, except near the end plates. The time-dependent positions of rows of high-contrast targets on a fin obtained by using video-grammetric deformation measurement technique [40,41] showed that the differences in the normal positions (y coordinates) of targets between different spanwise locations at a given moment were less than 15%. The streamwise and spanwise positions of targets were largely unchanged in small fin deformation. Therefore, the first eigenfunction is sufficient to describe the deformation of the major portion of the fin near the centerline. The normalized displacement of a thin fin is expressed as $w(x_3)/l = \eta_1(t)X_1(x_3)$, where x_3 is the coordinate along the incoming flow from the root of the fin and $\eta_1(t)$ are the time-dependent amplitude. The first characteristic beam function is

$$X_1(x_3) = \cos\gamma_1\bar{x} - \cosh\gamma_1\bar{x} + k_1(\sin\gamma_1\bar{x} - \sinh\gamma_1\bar{x})$$

where $k_1 = (\sin\gamma_1 - \sinh\gamma_1)/(\cos\gamma_1 + \cosh\gamma_1)$, $\bar{x} = x_3/l$ is the coordinate normalized by the fin length and $\gamma_1 = 1.875$. By using $w(x_3)/l = \eta_1(t)X_1(x_3)$ for least-squares fit to the detected fin edges, the time-dependent amplitude $\eta_1(t)$ is determined. Figure 17 shows the time-dependent deformation amplitude $\eta_1(t)$ and its power spectrum for the flexible fin located at $0.1c$ for AOA of 18°. The dominant spectral peak is at 1.3 Hz and the secondary peak is at 0.12 Hz. Similar spectra are found for AOA of 14, 16, and 20°. In general, the fin amplitude has a dominant component around 1.3 Hz

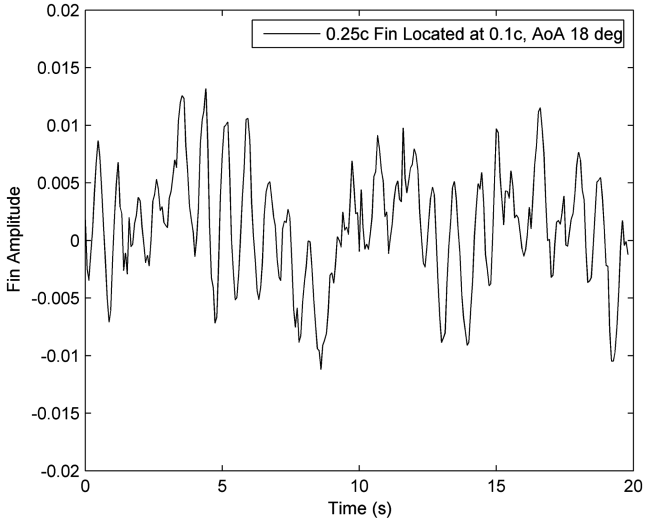

a)

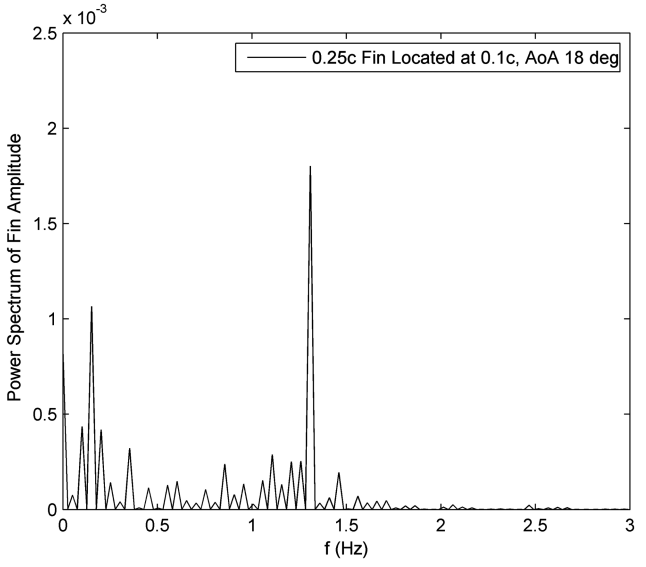

b)

Fig. 17 Amplitude of fin deformation: a) time trace and b) power spectrum of the fin amplitude.

and some low-frequency components in a range of 0.07–0.25 Hz. The frequency of 1.3 Hz corresponds to the Strouhal number based on the median momentum thickness of the shear layer (8 mm) is 0.041 that is close to the most unstable mode of the Strouhal number of 0.032. This indicates that the flexible fin is more responsive to the shear-layer mode. To determine the natural frequency of the flexible fin, the response of the fin to impulse forcing was measured in situ in still water in the water tunnel. It is found that the natural frequency of the flexible fin is 0.8 Hz, which is close to the shear-layer mode.

The velocity fields near the flexible fin are obtained from PIV measurements. The power spectra of U have the significant peaks at 0.1, 0.5, and 1.3 Hz on the upper side of the fin in $x''/c = 0.27$–0.39, which is approximately within the extent of the fin. Although a number of the spectral peaks exist, however, the spectra of U do not clearly systematically show the most dominant component across the fin. In contrast, the spectra of V have the significant peaks around 1.3 Hz that corresponds to the shear-layer mode. Note that the correlation processing is applied to the selected regions near the fin in PIV images, and velocity data obtained by the PIV software in the immediate neighborhoods of the fin are almost zero.

To provide a direct connection between the kinematics of fin deformation and the surrounding unsteady flow, the velocity is averaged over a narrow zone around the fin ($0.25 \le x''/c \le 0.4$ and $-0.05 \le y''/c \le 0.05$). Figure 18 shows the time traces of the

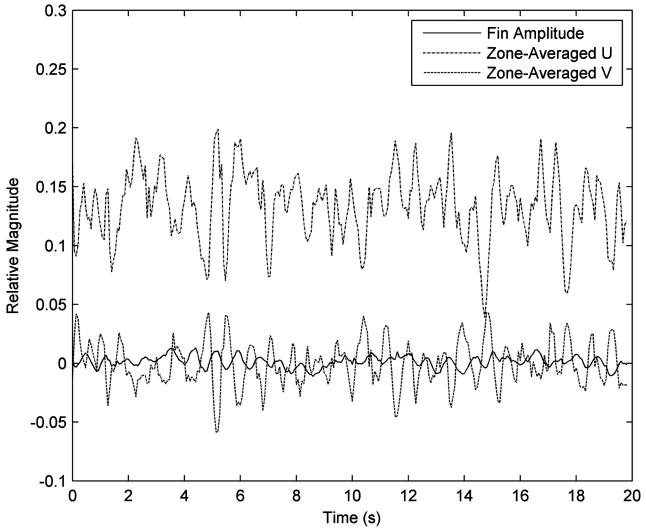

Fig. 18 Time traces of the relative fin deformation amplitude and zone-averaged velocity components around the fin, where the fin deformation amplitude and velocities are normalized by the fin length and the freestream velocity, respectively.

relative fin deformation amplitude and the zone-averaged velocity components U and V, where the fin deformation amplitude and velocities are normalized by the fin length and the freestream velocity, respectively. The waveform of the fin deformation amplitude approximately corresponds to that of the zone-averaged velocities, except that there are phase shifts between them. Further, the magnitude-squared coherences between the fin deformation amplitude and the zone-averaged velocity components $C_{\eta_1 U}$ and $C_{\eta_1 V}$ are calculated, where $\eta_1(t)$ is the fin deformation amplitude, and U and V are the zone-averaged velocity components. The definition of $C_{\eta_1 U}$ is $C_{\eta_1 U} = |P_{\eta_1 U}(f)|^2 / P_{\eta_1 \eta_1}(f) P_{UU}(f)$, where $P_{\eta_1 U}(f)$ is the cross power spectral density, and $P_{\eta_1 \eta_1}(f)$ and $P_{UU}(f)$ are the power spectral densities. $C_{\eta_1 V}$ is similarly defined. Figure 19 shows the magnitude-squared coherence between the fin amplitude and the zone-averaged velocity components. For both U and V, the dominant peaks in the magnitude-squared coherence are in a range of 1 to 1.7 Hz, indicating high correlation between the fin deformation amplitude and velocities at the shear-layer mode. The phase differences between the fin deformation amplitude $\eta_1(t)$ and the zone-averaged velocity components U and V around the fin are 14 and 149°, respectively.

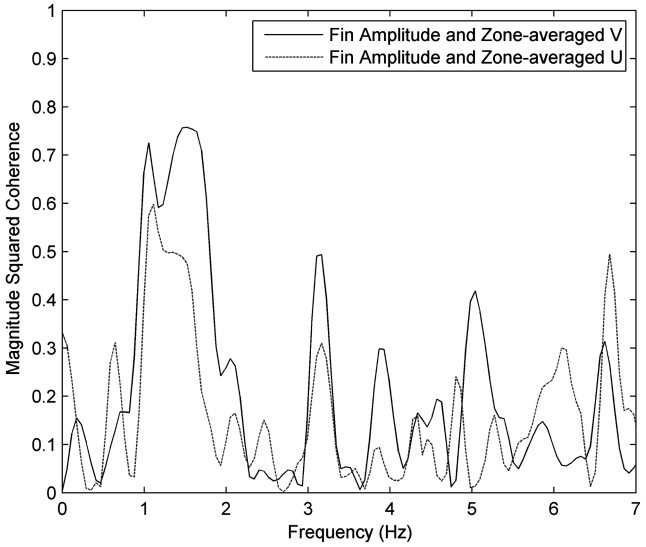

Fig. 19 Magnitude-squared coherence between the fin deformation amplitude and zone-averaged velocity components.

VI. Conclusions

Force measurements indicate that the drag of a NACA0012 airfoil model is reduced and the natural low-frequency oscillation is suppressed in poststall flows by using a thin flexible polymer fin attached to the supper surface near the leading edge. Because of the presence of a flexible fin, the velocity deficit and the momentum loss in the separated-flow region are reduced, and the recirculating flow at the time-average sense near the trailing edge is largely weakened and shifted downstream. However, the lift is reduced in poststall flows, since the organized lift-generating vortical structures in the separated shear layer are suppressed as well. The spectral analyses of the velocity fields show that the dominant low-frequency oscillation at the Strouhal number of 0.022 and other spectral components including the shear-layer mode are suppressed by the flexible fin.

Furthermore, the generating and controlling mechanisms of the low-frequency oscillation in poststall flows over the NACA0012 airfoil model are explored. It is found that the development of the vortical structures due to the Kelvin–Helmholtz instability in the shear layer coexists with the low-frequency oscillation. The evolution of the vortical structures is mainly detected in the shear layer near the leading edge. In contrast, the low-frequency oscillation is a global phenomenon in the entire separated-flow region. The short-time-averaged velocity fields reveal that the low-frequency oscillation is associated with the periodic development of the recirculating flow induced by the vortical structures developed in the shear layer. The relationship between the kinematics of deformation of the flexible fin and the surrounding unsteady flow is studied. The flexible fin is mainly responsive to the shear-layer mode and it is also affected passively by the low-frequency oscillation. The development of the organized vortical structures in the shear layer is considerably dampened by the flexible fin. As a result, the low-frequency oscillation is largely eliminated and the drag is reduced in poststall flows.

Acknowledgments

This work was supported by the U.S. Air Force Office of Scientific Research under grant number FA9550-06-1-0187.

References

[1] Glezer, A., and Amitay, M., "Synthetic Jets," *Annual Review of Fluid Mechanics*, 2002, pp. 503–529.
doi:10.1146/annurev.fluid.34.090501.094913

[2] Mittal, R., Kotapati, R. B., and Cattafesta, L. N., "Numerical Study of Resonant Interactions and Flow Control in a Canonical Separated Flow," AIAA Paper 2005-1261, 2005.

[3] Post, M., and Corke, T. C., "Separation Control on High Angle of Attack Airfoil Using Plasma Actuators," *AIAA Journal*, Vol. 42, No. 11, 2004, pp. 2177–2184.
doi:10.2514/1.2929

[4] Patel, M., Sowle, Z. H., Corke, T. C., and He, C., "Autonomous Sensing and Control of Wing Stall Using A Smart Plasma Slat," *Journal of Aircraft*, Vol. 44, No. 2, 2007, pp. 516–527.
doi:10.2514/1.24057

[5] Seifert, A., Eliahu, S., Greenblatt, D., and Wygnanski, I., "Use of Piezoelectric Actuators for Airfoil Separation Control," *AIAA Journal*, Vol. 36, No. 8, 1998, pp. 1535–1537.
doi:10.2514/2.549

[6] Mathew, J., Song, Q., Sankar, V., Sheplak, M., and Cattafesta, L. N., "Optimized Design of Piezoelectric Flap Actuators for Active Flow Control," *AIAA Journal*, Vol. 44, No. 12, 2006, pp. 2919–2928.
doi:10.2514/1.19409

[7] Greenblatt, D., and Wygnanski, I. J., "The Control of Flow Separation by Periodic Excitation," *Progress in Aerospace Sciences*, Vol. 36, No. 7, 2000, pp. 487–545.
doi:10.1016/S0376-0421(00)00008-7

[8] Lin, J. C., Robinson, S. K., McGhee, R. J., and Valarezo, W. O., "Separation Control on High-Lift Airfoil via Micro-Vortex Generators," *Journal of Aircraft*, Vol. 31, No. 6, 1994, pp. 1317–1323.
doi:10.2514/3.46653

[9] Lin, J. C., Howard, F. G., Bushnell, D. M., and Selby, G. V., "Investigation of Several Passive and Active Methods for Turbulent Flow Separation Control," AIAA Paper 90-1598, 1990.

[10] Seifert, A., and Pack, G., "Oscillatory Control of Separation at High Reynolds Numbers," *AIAA Journal*, Vol. 37, No. 9, 1999, pp. 1062–1071.
doi:10.2514/2.834

[11] Atik, H., Kim, C. Y., Van Dommelen, L. L., and Walker, J. D. A., "Boundary-Layer Separation Control on a Thin Airfoil Using Local Suction," *Journal of Fluid Mechanics*, Vol. 535, 2005, pp. 415–443.
doi:10.1017/S002211200500501X

[12] Munday, D., and Jacob, J., "Active Control of Separation on a Wing with Oscillating Camber," *Journal of Aircraft*, Vol. 39, No. 1, 2002, pp. 187–189.
doi:10.2514/2.2915

[13] Gad-el-Hak, M., *Flow Control: Passive, Active and Reactive Flow Management*, Cambridge Univ. Press, New York, 2000, Chap. 8.

[14] Collis, S. S., Joslin, R. D., Seifert, A., and Theofilis, V., "Issues in Active Flow Control: Theory, Control, Simulation, and Experiment," *Progress in Aerospace Sciences*, Vol. 40, Nos. 4–5, 2004, pp. 237–289.
doi:10.1016/j.paerosci.2004.06.001

[15] Zaman, K. B. M. Q., McKinzie, D. J., and Rumsey, C. L., "A Natural Low-Frequency Oscillation of the Flow over an Airfoil Near Stalling Conditions," *Journal of Fluid Mechanics*, Vol. 202, No. 1, 1989, pp. 403–442.
doi:10.1017/S0022112089001230

[16] Bragg, M. B., Heinrich, D. C., and Khodadoust, A., "Low-Frequency Flow Oscillation over Airfoils Near Stall," *AIAA Journal*, Vol. 31, No. 7, 1993, pp. 1341–1343.
doi:10.2514/3.49069

[17] Bragg, M. B., Heinrich, D. C., Balow, F. A., and Zaman, K. B. M. Q., "Flow Oscillation over an Airfoil Near Stall," *AIAA Journal*, Vol. 34, No. 1, 1996, pp. 199–201.
doi:10.2514/3.13045

[18] Broeren, A. P., and Bragg, M. B., "Flowfield Measurements over an Airfoil During Natural Low-Frequency Oscillations Near Stall," *AIAA Journal*, Vol. 37, No. 1, 1999, pp. 130–132.
doi:10.2514/2.678

[19] Broeren, A. P., and Bragg, M. B., "Unsteady Stalling of Thin Airfoils," *Fixed and Flapping Wing Aerodynamics for Micro Air Vehicle Applications*, edited by T. J. Mueller, AIAA, Reston, VA, 2001, Chap. 10.

[20] Mukai, J., Enomoto, S., and Aoyama, T., "Large-Eddy Simulation of Natural Low-Frequency Flow Oscillations on an Airfoil Near Stall," AIAA Paper 2006-1417, 2006.

[21] Wu, J.-Z., Lu, X-Y., Denny, A. G., Fan, M., and Wu, J.-M., "Post-Stall Flow Control on an Airfoil by Local Unsteady Forcing," *Journal of Fluid Mechanics*, Vol. 371, 1998, pp. 21–58.

[22] Loftin, L. K., and Smith, H. A., "Aerodynamic Characteristics of 15 NACA Airfoil Sections at Seven Reynolds Numbers from 0.7×10^6 to 9.0×10^6," NACA TN 1945, 1949.

[23] Selig, M., Guglielmo, J., Broeren, A. P., and Giguere, P., *Summary of Low-Speed Airfoil Data*, Vols. 1–3, SoarTech, Virginia Beach, VA, 1995.

[24] Laitone, E. V., "Wind Tunnel Tests of Wings at Reynolds Numbers Below 70,000," *Experiments in Fluids*, Vol. 23, No. 5, 1997, pp. 405–409.
doi:10.1007/s003480050128

[25] Kunz, P. J., and Kroo, I., "Analysis and Design of Airfoils for Use at Ultra-Low Reynolds Numbers," *Fixed and Flapping Wing Aerodynamics for Micro Air Vehicle Applications*, edited by T. J. Mueller, AIAA Press, Reston, VA, 2001, Chap. 3.

[26] Sunada, S., Ozaki, K., Tanaka, M., Yasuda, T., Yasuda, K., and Kawachi, K., "Airfoil Characteristics at a Low Reynolds Number," *Journal of Flow Visualization and Image Processing*, Vol. 7, 2000, pp. 207–215.

[27] Zaman, K. B. M. Q., "Effects of Acoustic Excitation on Stalled Flows over an Airfoil," *AIAA Journal*, Vol. 30, No. 6, 1992, pp. 1492–1499.
doi:10.2514/3.11092

[28] Bechert, D. W., Bruse, M., Hage, W., and Meyer, R., "Fluid Mechanics of Biological Surfaces and Their Technological Application," *Naturwissenschaften*, Vol. 87, No. 4, 2000, pp. 157–171.
doi:10.1007/s001140050696

[29] Bramesfeld, G., and Maughmer, M. D., "Experimental Investigation of Self-Actuating, Upper-Surface, High-Lift-Enhancing Effectors," *Journal of Aircraft*, Vol. 39, No. 1, 2002, pp. 120–124.
doi:10.2514/2.2905

[30] Meyer, R., Hage, W., Bechert, D. W., Schatz, M., Knacke, T., and Thiele, F., "Separation Control by Self-Activated Movable Flaps," *AIAA Journal*, Vol. 45, No. 1, 2007, pp. 191–199.
doi:10.2514/1.23507

[31] Rinoie, K., Okuno, M., and Sunada, Y., "Airfoil Stall Suppression by Use of a Bubble Burst Control Plate," *AIAA Journal*, Vol. 47, No. 2, 2009, pp. 322–330.
doi:10.2514/1.37352
[32] Meirovitch, L., *Analytical Methods in Vibrations*, Macmillan, New York, 1967.
[33] Liu, T., Montefort, J., Liou, W., Pantula, S. R., and Shams, Q. A., "Lift Enhancement by Static Extended Trailing Edge," *Journal of Aircraft*, Vol. 44, No. 6, 2007, pp. 1939–1947.
doi:10.2514/1.31995
[34] Stanislas, M., Okamoto, K., Kahler, C. J., and Westerweel, J., "Main Results of the Second International PIV Challenge," *Experiments in Fluids*, Vol. 39, No. 2, 2005, pp. 170–191.
doi:10.1007/s00348-005-0951-2
[35] Pantula, S. R., "Modeling Fluid Structure Interaction over a Flexible Fin Attached to a NACA0012 Airfoil," Ph.D. Thesis, Dept. of Mechanical and Aeronautical Engineering, Western Michigan Univ., Kalamazoo, MI, 2008.
[36] Carr, L. W., "Progress in Analysis and Prediction of Dynamic Stall," *Journal of Aircraft*, Vol. 25, No. 1, 1988, pp. 6–17.
doi:10.2514/3.45534
[37] Saffman, P. G., and Sheffield, J. S., "Flow over a Wing with an Attached Free Vortex," *Studies in Applied Mathematics*, Vol. 57, 1977, pp. 107–117.
[38] Huang, M. K., and Chow, C. Y., "Trapping of a Free Vortex by Joukowski Airfoils," *AIAA Journal*, Vol. 20, No. 3, 1982, pp. 292–298.
doi:10.2514/3.7913
[39] Liu, T., Montefort, J., Liou, W., Pantula, R., and Shams, Q., "Post-Stall Flow Control Using a Flexible Fin on Airfoil," AIAA Paper 2009-1106, 2009.
[40] Liu, T., Cattafesta, L., Radezsky, R., and Burner, A. W., "Photogrammetry Applied to Wind Tunnel Testing," *AIAA Journal*, Vol. 38, No. 6, 2000, pp. 964–971.
doi:10.2514/2.1079
[41] Burner, A., and Liu, T., "Videogrammetric Model Deformation Measurement Technique," *Journal of Aircraft*, Vol. 38, No. 4, 2001, pp. 745–754.
doi:10.2514/2.2826

A. Naguib
Associate Editor